462 KSME Journal, Vol. 9, No. 4, pp. 462~471, 1995

Optimal Synthesis of a Wrist-Type 6 Degree-of-Freedom Force/Torque Sensor Using Stewart Platform Structure

Whee-Kuk Kim*, Kum-Kang Huh*, Byung-Ju Yi and Whang Cho*****

(Received March 23, 1995)

The F/T sensor investigated in this study utilizes the Stewart Platform Mechanism Structure. Normally-employed 6-prismatic joints are replaced by 6-prismatic bars, which are extensible and compressible only along the axial direction of the bars. The complete analyses for the design of this kind of F/T sensor are conducted: the position analysis, the first-order and second-order kinematic analyses, and the force-deformation analysis based on the first-order kinematic characteristics of the system. Lastly, a dimensional synthesis for the F/T sensor is performed based on the kinematic isotropic index.

Key Words: Stewart Platform, F/T Sensor, Parallel Mechanism.

1. Introduction

Most of current wrist-type F/T sensors are designed to have various shaped structures of elastic members, on which more than six strain gauges are attached to measure six independent forces. For example, a Scheinman F/T sensor utilizes deformation of elastic members, where each of two rectangular shaped elastic bars cross perpendicularly each other (called Maltese Cross Webbing)(Shimano and Roth, 1978). SRI F/T sensors are made of a tube-shaped aluminum and also properly cut to have eight narrow neck-shaped elastic beams to minimize cross coupling effects. (Kak and Albus, 1985) Yabuki made a F/T sensor using eight parallel leaf springs, each of which is designed to have a deformation particularly along one direction. (Yabuki, 1990) Yoshikawa and Miyazaki (1989) designed a F/T sensor using parallel plate structure. Each of three plates are combined mutually perpendicular each other to reduce cross coupling effects. Currently, most of commercialized wrist-type F/T sensors belong to this kind of F/T sensors (i.e., Lord F/T sensor, JR3 F/T sensor, etc.).

Several performance criteria of F/T sensors are suggested; Nakamura proposed three criteria such as strain gauge sentivity, force sensitivity, and minimum stiffness, (Nakamura, et al.) and Uchiyama et. al. (1991), used the condition number of the strain compliance matrix. Recently, Svinin and Uchiyama (1994) presented a generalized model and its systematic analysis of force sensors with parallel connection of elastic elements at the design stage. They found partial solutions of the optimization problem for the regular-polyhedron-form-based sensors.

Recently, a 6-degree-of-freedom F/T sensor using Stewart Platform Structure shown in Fig. 1 is appeared in literature (Negen, et al, 1992; Ma and Angeles, 1992; Reboulet and Pigeyre, 1992). This F/T sensor places linear springs with known spring constant inside the prismatic joints and is equipped with six LVDTs (linear voltage differential transformer) to measure displacements of each of six prismatic joints. Therefore, the applied force to the sensor can be computed directly using the displacements of springs. Note that in this type of F/T sensors, each prismatic joint only experiences force along the axial direction. It is expected that this type of F/T sensors might have

* Department of Control and Instrumentation Engineering, Korea University

** Department of Control and Instrumentation Engineering, Hanyang University

*** Department of Control and Instrumentation Engineering, Kwangwoon University

an excellent performance as an F/T sensor.

In this study, we focus on the complete kinematic analyses, and optimal systhesis of F/T sensors using Stewart Platform structure (Uchiyama et al, 1991; Nguyen et al, 1992), which are related to computing external forces applied to the upper plate and investigating chracteristics as a F/T sensor, are described.

2. Kinematic Analysis of F/T Sensor using Stewart Platform Structure

Assume that all of prismatic joints of Stewart Platform mechanism are replaced by prismatic bars each of which is restricted to be deformable only along the axial direction of bars, and other components such as an upper plate and a lower (or base) plate are rigid. When external forces are applied to the upper plate, force felt at each prismatic bar can be computed directly using kinematic relations of this mechanism. In this section, geometric description, position analysis, first-order and second-order kinematic analyses of this mechanism are briefly described.

2.1 Description of a F/T Sensor

F/T sensor mechanism consists of an upper plate, a base plate, and six prismatic bars connecting an upper plate to a base plate as shown in Fig. 1. First, define (x_b, y_b, z_b) as the base frame which is fixed to the base plate and has the origin at the center of the plate. Let R_i be the position vector from the origin of the base frame to the intersection point on a base plate with one of six prismatic bars, where a 2-dof universal joint is placed. Likewise, define (x_t, y_t, z_t) as the upper plate frame which is fixed in the upper plate and has the origin at the center of the plate. Let $r^{(T)}$ be the local position vector, represented in an upper plate frame, from the origin of the upper plate frame to the intersection point on an upper plate, where a 3-dof ball & socket joint is placed. Let $l=(l_1\ l_2\ \cdots l_6)^T$ represent the deformational linear displacement of prismatic bars. Let $R_t=(R_{tx}\ R_{ty}\ R_{tz})^T$ be the absolute position vector, represented in a base frame, from the origin of the base frame to the origin of the upper plate frame.

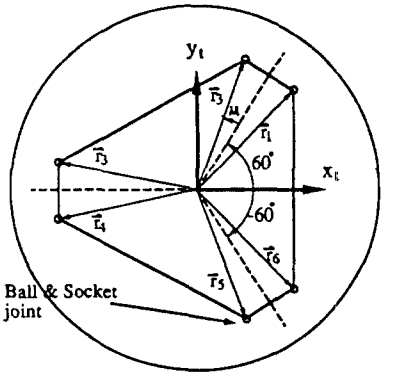

a) Top plate

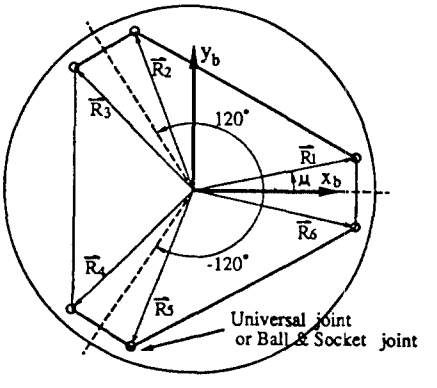

b) Base plate

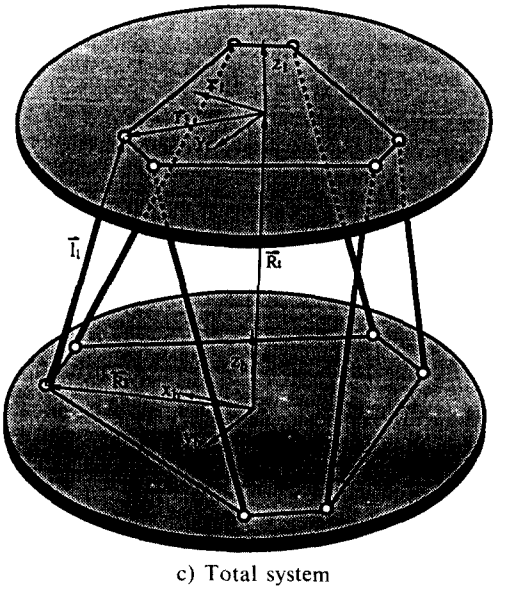

c) Total system

Fig. 1 Stewart Platform System

And let $[{}^{B}_{T}R]$ be the transformation matrix from the base frame to the upper plate frame. Transformation matrix which represents the orientation of the upper frame is represented by three Roll-Pitch-Yaw angles. That is,

$$[{}^{B}_{T}R]=Rot(z,\ a)\ \ Rot(y,\ \beta)\ \ Rot(x,\ \gamma) \tag{1}$$

To maintain symmetric configuration of the mechanism, six intersection points on the base plate lie on the circle of radius R and at $\pm\mu°$ from three reference angles (i.e., 0°, 120° and 240°), respectively, as shown in Fig. 1. Likewise, six intersection points on an upper plate lie on the circle of radius r and at $\pm\mu^0$ from one of three reference angles (i.e., 60°, 180° and 300°), respectively. Therefore, the absolute position vectors from the origin of the base plate to each intersection point on the base plate can be written as

$$\boldsymbol{R}_1=(R\cos\mu\ \ R\sin\mu\ \ 0)^T \tag{2}$$
$$\boldsymbol{R}_2=(R\cos(120-\mu)\ \ R\sin(120-\mu)\ \ 0)^T \tag{3}$$
$$\boldsymbol{R}_3=(R\cos(120+\mu)\ \ R\sin(120+\mu)\ \ 0)^T \tag{4}$$
$$\boldsymbol{R}_4=(R\cos(240-\mu)\ \ R\sin(240-\mu)\ \ 0)^T \tag{5}$$
$$\boldsymbol{R}_5=(R\cos(240+\mu)\ \ R\sin(240+\mu)\ \ 0)^T \tag{6}$$
$$\boldsymbol{R}_6=(R\cos(-\mu)\ \ R\sin(-\mu)\ \ 0)^T, \tag{7}$$

and local position vectors from the origin of the upper frame to each of six intersection points on the upper plate in upper plate frame can be expressed as

$$\boldsymbol{r}_1^{(T)}=(r\cos(60-\mu)\ \ r\sin(60-\mu)\ \ 0)^T \tag{8}$$
$$\boldsymbol{r}_2^{(T)}=(r\cos(60+\mu)\ \ r\sin(60+\mu)\ \ 0)^T \tag{9}$$

$$\boldsymbol{r}_3^{(T)}=(r\cos(180-\mu)\ \ r\sin(180-\mu)\ \ 0)^T \tag{10}$$
$$\boldsymbol{r}_4^{(T)}=(r\cos(180+\mu)\ \ r\sin(180+\mu)\ \ 0)^T \tag{11}$$
$$\boldsymbol{r}_5^{(T)}=(r\cos(300-\mu)\ \ r\sin(300-\mu)\ \ 0)^T \tag{12}$$
$$\boldsymbol{r}_6^{(T)}=(r\cos(300+\mu)\ \ r\sin(300+\mu)\ \ 0)^T. \tag{13}$$

Note that the mechanism maintains perfect symmetric configuration when all output variables are set to 0.

2.2 Position analysis

In Fig. 1, the position vector from the origin of the base frame to the origin of the upper plate frame can be written as

$$\boldsymbol{R}_t=\boldsymbol{R}_i+\boldsymbol{l}_i-\boldsymbol{r}_i \text{ for } i=1,\ 2,\cdots,\ 6 \tag{14}$$

where

$$\boldsymbol{r}_i=[{}^{B}_{T}R]\boldsymbol{r}_i^{(T)} \tag{15}$$

represents the absolute position vector of $\boldsymbol{r}_i^{(T)}$ expressed in the base frame and $\boldsymbol{l}_i$ represents the position vector from the intersection point on the base frame to the intersection point on the upper plate along axial direction of the ith prismatic bar.

2.2.1. Reverse position analysis

Eq. (14) can be rearranged in terms of $\boldsymbol{l}_i$ as

$$\boldsymbol{l}_i=\boldsymbol{R}_t+\boldsymbol{r}_i-\boldsymbol{R}_i \tag{16}$$

When $\boldsymbol{R}_t$ and $[{}^{B}_{T}R]$ are given, l_i can be found directly from

$$l_i=\sqrt{\boldsymbol{l}_i\cdot\boldsymbol{l}_i}$$
$$=\sqrt{(\boldsymbol{R}_t+\boldsymbol{r}_i-\boldsymbol{R}_i)\cdot(\boldsymbol{R}_t+\boldsymbol{r}_i-\boldsymbol{R}_i)}. \tag{17}$$

2.2.2 Forward position analysis

When l_i for $i=1,\ 2,\ \ldots\ 6$ are given, $\boldsymbol{R}_t$ and $[{}^{B}_{T}R]$ can be found by solving the following six simultaneous equations, numerically (for example, using Newton Rhapson's method (Nguyen et al., 1992)):

$$f_i=(\boldsymbol{R}_t-\boldsymbol{R}_i+[{}^{B}_{T}R]\boldsymbol{r}_i^{(T)})\cdot(\boldsymbol{R}_t-\boldsymbol{R}_i+[{}^{B}_{T}R]\boldsymbol{r}_i^{(T)})-l_i^2$$
$$=0 \text{ for } i=1,\ 2,\ \cdots,\ 6 \tag{18}$$

2.3. First-order kinematic model

Let the angular and translational velocity vector of the upper plate be represented, respectively, as

$$\boldsymbol{\omega}=[\omega_x\ \ \omega_y\ \ \omega_z]^T, \tag{19}$$
$$\dot{\boldsymbol{R}}_t=[\dot{R}_{tx}\ \ \dot{R}_{ty}\ \ \dot{R}_{tz}]^T. \tag{20}$$

Squaring Eq. (17) and differentiating the results with respect to time yields

$$l_i\dot{l}_i=\dot{\boldsymbol{R}}_i\cdot(\boldsymbol{R}_t+\boldsymbol{r}_i-\boldsymbol{R}_i)+\dot{\boldsymbol{r}}_i\cdot(\boldsymbol{R}_t+\boldsymbol{r}_i-\boldsymbol{R}_i)-\dot{\boldsymbol{R}}_i\cdot(\boldsymbol{R}_t+\boldsymbol{r}_i-\boldsymbol{R}_i) \tag{21}$$

Noting that $\boldsymbol{R}_i$ is constant, and that

$$\dot{\boldsymbol{r}}_i=\boldsymbol{\omega}\times\boldsymbol{r}_i \tag{22}$$

and

$$\boldsymbol{r}_i\times\boldsymbol{r}_i=0, \tag{23}$$

the second term of the right-hand side of Eq. (21) can be rewritten as

$$\begin{aligned}&\dot{\boldsymbol{r}}_i \cdot (\boldsymbol{R}_t + \boldsymbol{r}_i - \boldsymbol{R}_i)\\ &= (\boldsymbol{\omega} \times \boldsymbol{r}_i) \cdot (\boldsymbol{R}_t - \boldsymbol{R}_i)\\ &= \boldsymbol{r}_i \times (\boldsymbol{R}_t - \boldsymbol{R}_i) \cdot \boldsymbol{\omega}. \end{aligned} \tag{24}$$

Therefore, Eq. (21) can be expressed in terms of velocity vectors of the upper plate as

$$\begin{aligned}l_i \dot{l}_i &= (\boldsymbol{R}_t + \boldsymbol{r}_i - \boldsymbol{R}_i) \cdot \dot{\boldsymbol{R}}_t\\ &\quad + \boldsymbol{r}_i \times (\boldsymbol{R}_t - \boldsymbol{R}_i) \cdot \boldsymbol{\omega}\\ &= \boldsymbol{l}_i \cdot \dot{\boldsymbol{R}}_t + (\boldsymbol{r}_i \times \boldsymbol{l}_i) \cdot \boldsymbol{\omega}. \end{aligned} \tag{25}$$

It can be further simplified in a matrix form as

$$[L]\,\dot{\boldsymbol{l}} = [A]\,\dot{\boldsymbol{u}} \tag{26}$$

where

$$\dot{\boldsymbol{l}} = (\dot{l}_1 \;\; \dot{l}_2 \;\; \dot{l}_3 \;\; \dot{l}_4 \;\; \dot{l}_5 \;\; \dot{l}_6)^T \tag{27}$$

$$\dot{\boldsymbol{u}} = [\dot{\boldsymbol{R}}_t \;\; \boldsymbol{\omega}]^T = [\dot{x} \;\; \dot{y} \;\; \dot{z} \;\; \boldsymbol{\omega}_x \;\; \boldsymbol{\omega}_y \;\; \boldsymbol{\omega}_z]^T \tag{28}$$

$$[L] = diag(l_1 \;\; l_2 \;\; l_3 \;\; l_4 \;\; l_5 \;\; l_6) \tag{29}$$

$$[A] = \begin{bmatrix} \boldsymbol{l}_1^T & (\boldsymbol{r}_1 \times \boldsymbol{l}_1)^T \\ \boldsymbol{l}_2^T & (\boldsymbol{r}_2 \times \boldsymbol{l}_2)^T \\ \vdots & \vdots \\ \boldsymbol{l}_6^T & (\boldsymbol{r}_6 \times \boldsymbol{l}_6)^T \end{bmatrix} \tag{30}$$

When $[A]$ is not singular, the inverse relation for Eq. (26) holds as

$$\dot{\boldsymbol{u}} = [G_l^u]\,\dot{\boldsymbol{l}} \tag{31}$$

where

$$[G_l^u] = [A]^{-1}[L] \tag{32}$$

represents a Jacobian matrix or sometimes is called as a first-order kinematic influence coefficient matrix. Note that the subscript and the superscript of $[G_l^u]$ represents the independent variables (l) and the dependent variables (u), respectively.

When $[G_l^u]$ is not singular, the inverse relation of Eq. (31) is obtained as

$$\dot{\boldsymbol{l}} = [G_l^u]\,\dot{\boldsymbol{u}} \tag{33}$$

where

$$[G_u^l] = [G_l^u]^{-1} = \begin{bmatrix} \hat{\boldsymbol{l}}_1^T & (\boldsymbol{r}_1 \times \hat{\boldsymbol{l}}_1)^T \\ \hat{\boldsymbol{l}}_2^T & (\boldsymbol{r}_2 \times \hat{\boldsymbol{l}}_2)^T \\ \vdots & \vdots \\ \hat{\boldsymbol{l}}_6^T & (\boldsymbol{r}_6 \times \hat{\boldsymbol{l}}_6)^T \end{bmatrix}. \tag{34}$$

$$[H_{uu}^{l_i}] = \frac{1}{l_i}\begin{bmatrix} [I] - \hat{\boldsymbol{l}}_i \hat{\boldsymbol{l}}_i^T \\ (\boldsymbol{r}_i \times) - (\boldsymbol{r}_i \times \hat{\boldsymbol{l}}_i)\,\hat{\boldsymbol{l}}_i^T \;\; (\boldsymbol{l}_i - \boldsymbol{r}_i)\,\boldsymbol{r}_i^T \end{bmatrix}$$

From Eqs. (31) and (39), the acceleration of the upper plate can be obtained as

$$\ddot{\boldsymbol{u}} = [G_u^l]^{-1}\{\ddot{\boldsymbol{l}} - \dot{\boldsymbol{u}}^T[H_{uu}^l]\,\dot{\boldsymbol{u}}\}$$

In the above equation, $\hat{\boldsymbol{l}}_i = \boldsymbol{l}_i / l_i$ represents unit vectors along the axial direction of each prismatic bar.

2.4 Second-order kinematic model

Again, differentiating Eq. (25) with respect to time yields

$$\begin{aligned}l_i \ddot{l}_i &= \boldsymbol{l}_i \cdot \ddot{\boldsymbol{R}}_t + (\boldsymbol{r}_i \times \boldsymbol{l}_i) \cdot \dot{\boldsymbol{\omega}} + \dot{\boldsymbol{l}}_i \cdot \dot{\boldsymbol{R}}_t\\ &\quad + \frac{d}{dt}(\boldsymbol{r}_i \times \boldsymbol{l}_i) \cdot \boldsymbol{\omega} - \dot{l}_i^2\\ &\quad \text{for } i = 1, 2, \cdots, 6 \end{aligned} \tag{35}$$

where

$$\dot{\boldsymbol{l}}_i \cdot \dot{\boldsymbol{R}}_t = \dot{\boldsymbol{R}}_t^T \dot{\boldsymbol{R}}_t - \dot{\boldsymbol{R}}_t^T (\boldsymbol{r}_i \times \boldsymbol{\omega}) \tag{36}$$

$$\begin{aligned}&\frac{d}{dt}(\boldsymbol{r}_i \times \boldsymbol{l}_i) \cdot \boldsymbol{\omega}\\ &= \boldsymbol{\omega}^T (\boldsymbol{r}_i \times \dot{\boldsymbol{R}}_t) + \boldsymbol{\omega}^T [(\boldsymbol{l}_i - \boldsymbol{r}_i)\,\boldsymbol{r}_i^T\\ &\quad - [I](\boldsymbol{l}_i - \boldsymbol{r}_i)^T \boldsymbol{r}_i]\boldsymbol{\omega} \end{aligned} \tag{37}$$

and

$$\begin{aligned}\dot{l}_i^2 &= \dot{\boldsymbol{R}}_t^T \hat{\boldsymbol{l}}_i \hat{\boldsymbol{l}}_i^T \dot{\boldsymbol{R}}_t\\ &\quad + \boldsymbol{\omega}^T (\boldsymbol{r}_i \times \hat{\boldsymbol{l}}_i)^T (\boldsymbol{r}_i \times \hat{\boldsymbol{l}}_i)\,\boldsymbol{\omega}\\ &\quad + \dot{\boldsymbol{R}}_t^T \hat{\boldsymbol{l}}_i (\boldsymbol{r}_i \times \hat{\boldsymbol{l}}_i)^T \boldsymbol{\omega}\\ &\quad + \boldsymbol{\omega}^T (\boldsymbol{r}_i \times \hat{\boldsymbol{l}}_i)^T \hat{\boldsymbol{l}}_i \dot{\boldsymbol{R}}_t. \end{aligned} \tag{38}$$

Therefore, these equations for each prismatic bar altogether can be written in a matrix form as

$$\ddot{\boldsymbol{l}} = [G_u^l]\,\ddot{\boldsymbol{u}} + \dot{\boldsymbol{u}}_T [H_{uu}^l]\,\dot{\boldsymbol{u}} \tag{39}$$

where

$$[H_{uu}^l] = \begin{bmatrix} [H_{uu}^{l_1}] \\ [H_{uu}^{l_2}] \\ \vdots \\ [H_{uu}^{l_6}] \end{bmatrix} \tag{40}$$

Equation (39) represents the inverse acceleration equation. Note that the subscript and the superscript of $[H_{uu}^l]$ represents the dependent variables (u) and the independent variables (l), respectively. $[H_{uu}^l]$ represents an inverse second-order kinematic influence coefficient matrix and is a 3-dimensional array consisting of six plane matrices, and each plane can be obtained as

$$\begin{bmatrix} (-\boldsymbol{r}_i \times) - \hat{\boldsymbol{l}}_i (\boldsymbol{r}_i \times \hat{\boldsymbol{l}}_i)^T \\ -[I](\boldsymbol{l}_i - \boldsymbol{r}_i)^T \boldsymbol{r}_i - (\boldsymbol{r}_i \times \hat{\boldsymbol{l}}_i)^T (\boldsymbol{r}_i \times \hat{\boldsymbol{l}}_i) \end{bmatrix} \tag{41}$$

$$\begin{aligned}&= [G_l^u]\,\ddot{\boldsymbol{l}} + \dot{\boldsymbol{u}}^T \{-[G_l^u] \cdot [H_{uu}^l]\}\,\dot{\boldsymbol{u}}\\ &= [G_l^u]\,\ddot{\boldsymbol{l}} + \dot{\boldsymbol{l}}^T [G_l^u]^T (-[G_l^u] \cdot [H_{uu}^l])[G_l^u]\,\dot{\boldsymbol{l}}. \end{aligned} \tag{42}$$

Noting that the forward acceleration equations can be represented in the same form as in Eq. (39), that is,

$$\ddot{\boldsymbol{u}}=[G_l^u]\,\ddot{\boldsymbol{l}}+\dot{\boldsymbol{l}}^T[H_{ll}^u]\,\dot{\boldsymbol{l}}, \tag{43}$$

the forward second-order kinematic influence coefficient array can be obtained as

$$[H_{ll}^u]=[G_l^u]^T(-[G_l^u]\cdot[H_{uu}^l])[G_l^u]. \tag{44}$$

The generalized dot product operator ($\cdot$) used in the above equation is defined as follows; when A and B is a $p\times q$ matrix and a 3 dimensional $q\times(m\times n)$ array, respectively, then the resulting 3-dimensional $p\times(m\times n)$ C array can be found as (Freeman and Tesar, 1988)

$$[C]_{pij}=[A\cdot B]_{pij}=\sum_{k=1}^{q}A_{pk}B_{kij}. \tag{45}$$

Lastly, it can be noted that $[H_{ll}^u]$ is defined as

$$\frac{d[G_l^u]}{dt}=\dot{\boldsymbol{l}}^T[H_{ll}^u] \tag{46}$$

and that it is related to the gradient of Jacobain($[G_l^u]$).

3. Force-Deformation Analysis

Let $\boldsymbol{\tau}=(f_1,\ \cdots\cdots,\ f_6)^T$ and $\boldsymbol{\delta l}=(\delta l_1,\ \cdots,\ \delta l_6)^T$ represents the axial force vector and virtual axial deformation vector along the prismatic bars, respectively. And let $\boldsymbol{f}=(f_x\ f_y\ f_j\ \tau_x\ \tau_y\ \tau_z)^T$ and $\boldsymbol{\delta u}=(\delta x\ \delta y\ \delta z\ \delta\theta_x\ \delta\theta_y\ \delta\theta_z)^T$ represents the external force/torque vector applied to the center of the upper plate and the virtual displacement vector of the upper plate, respectively. From principle of virtual work, the following relation holds

$$\boldsymbol{\tau}^T\boldsymbol{\delta l}=\boldsymbol{f}^T\boldsymbol{\delta u}. \tag{47}$$

Substituing Eq. (31) into Eq. (47) yields

$$\boldsymbol{f}=[G_u^l]^T\boldsymbol{\tau}. \tag{48}$$

Recall that six prismatic bars have sufficiently high stiffnesses along the other directions except along the axial direction. Now, axial stiffnesses of six prismatic bars are given as K_i (for $i=1, 2, \cdots 6$) and that actual deformations along axial direction of each prismatic bar (δl_i) can be measured via transducers such as strain gauge. The axial forces felt along each prismatic bar (when an external force is applied to the upper plate) can be obtained as

$$\boldsymbol{\tau}=[K]\boldsymbol{\delta l} \tag{49}$$

where $[K]$ is a diagonal stiffness matrix; that is,

$$[K]=diag[K_1,\ K_2,\ K_3,\ K_4,\ K_5,\ K_6]. \tag{50}$$

Using Eqs. (48) and (49), the relations between the external forces applied to the center of the upper plate and the deformations occurred at prismatic bars can be found as

$$\boldsymbol{f}=[G_u^l]^T[K]\boldsymbol{\delta l}. \tag{51}$$

In this equation, it is assumed that $\max|\delta l_i|$ is sufficiently small so that the effects from the change of Jacobian matrix is sufficiently small. This condition can be checked by investigating the second-order kinematic influence coefficient array ($[H_{ll}^u]$) obtained in Eq. (44).

The components of the external force vector are normalized with respect to their nominal values. For the normalized force vector, $\boldsymbol{f}^*=(f_x^*f_y^*f_z^*\tau_x^*\tau_y^*\tau_z^*)^T$, defined as

$$\begin{cases} f_x^*=\dfrac{f_x}{(f_x)_{\max}} \\ f_y^*=\dfrac{f_y}{(f_y)_{\max}} \\ f_z^*=\dfrac{f_z}{(f_z)_{\max}} \end{cases} \quad \begin{cases} \tau_x^*=\dfrac{\tau_x}{(\tau_x)_{\max}} \\ \tau_y^*=\dfrac{\tau_y}{(\tau_y)_{\max}} \\ \tau_z^*=\dfrac{\tau_z}{(\tau_z)_{\max}} \end{cases} \tag{52}$$

the joint deformation-to-external force relation can be written as

$$\boldsymbol{f}^*=([G_u^l]^T)^*\boldsymbol{\delta l} \tag{53}$$

where

$$([G_u^l]^T)^*=[S][G_u^l]^T[K] \tag{54}$$

represents the normalized compliance matrix and $[S]$ represents diagonal scale matrix written as

$$[S]=diag[1/f_{x\max},\ 1/f_{y\max},\ 1/f_{z\max},\ 1/\tau_{x\max},\ 1/\tau_{y\max},\ 1/\tau_{z\max}] \tag{55}$$

4. Geometric Characteristics of F/T Sensor

Kinematic characteristics can be examined by investigating characteristics of the Jacobian matrix in Eq. (31). Let the square of singular values of normalized compliance matrix $[S][G_u^l]^T[K]$ be written as

$$\sigma_{\min}^2=\sigma_1^2\le\cdots\le\sigma_6^2=\sigma_{\max}^2. \tag{56}$$

Then using Eq. (54) and Rayleigh's principle, the upper and lower limits of the ratio between the output force vector and joint deformation vector can be found as

$$\sigma_{\min}^2 \leq \frac{\delta \boldsymbol{l}^T([K]^T[G_u^l][S]^T[S][G_u^l]^T[K])\,\delta \boldsymbol{l}}{\delta \boldsymbol{l}^T \delta \boldsymbol{l}^T} \leq \sigma_{\max}^2. \tag{57}$$

This equation implies that when $\|\delta \boldsymbol{l}\|=1$, the magnitude of the force vector norm is greater than $\sigma_{\min}$ but less than $\sigma_{\max}$.

One of the ideal characteristics of F/T sensors is to have uniform output force-to-joint deformation transmision characteristics. This characteristics can be represented by isotropic index which is defined as

$$\sigma_{KI} = \frac{\sigma_{\min}([S][G_u^l]^T[K])}{\sigma_{\max}([S][G_u^l]^T[K])} \tag{58}$$

By definition the value of σ_{KI} can not be greater than 1. As the value of σ_{KI} gets close to 1, it represents uniform force transmission characteristics of the F/T sensor. When it gets close to 0, it represents non-uniform transmission charateristics.

5. Optimal design of F/T Sensor

To reduce the number of design parameters and to maintain symmetric configuration of the F/T sensor as possible, intersection points of the upper and the base plate with each prismatic bar are placed symmetrically. To make the two plates face each other in parallel, four out of six output variables of the upper plate are fixed as

$$R_{tx}=0,\ R_{ty}=0,\ \beta=0,\ \gamma=0. \tag{59}$$

Further, assume that both a scale matrix ($[S]$) and a stiffness matrix ($[K]$) are identity matrices. Physically, this implies that when all six prismatic bars are made of the same materials and have the same shapes, they must have the same length. Therefore, α representing rotation angle about z_t axis of the upper plate is set to 0°, noting that with this angle all six prismatic bars maintain the same length.

In these assumptions, design variables in optimization of F/T sensor are reduced down to three;

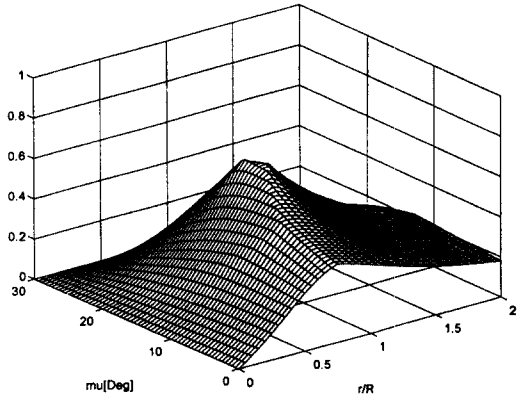

Fig. 3 Contour plot of $\sigma_{KI}([G_u^l])$ for $R_{tz}=0.5$

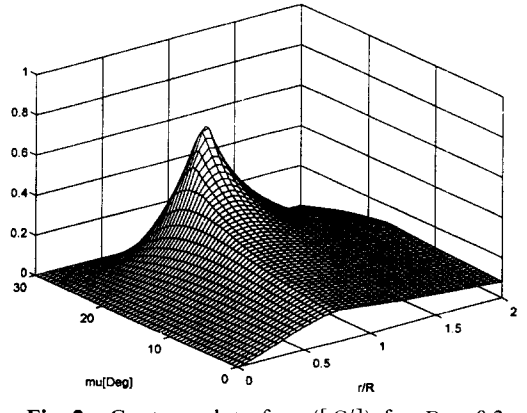

Fig. 2 Contour plot of $\sigma_{KI}([G_u^l])$ for $R_{tz}=0.2$

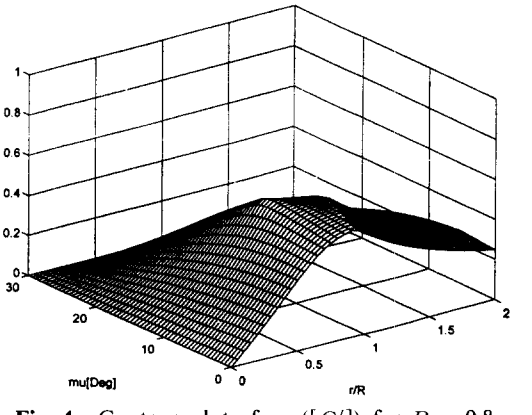

Fig. 4 Contour plot of $\sigma_{KI}([G_u^l])$ for $R_{tz}=0.8$

that is, one output variable of the upper plate (R_{tz}, the displacement along $\dot{z}_b$ axis) and two geometric variables (r/R and μ).

Figure 2, 3 and 4 represent 3-D plots of isotropic index of $[G_u^t]$ for the fixed $R_{tz}=0.2$, 0.5, 0.8 with respect to two remaining variables (r/R and μ), respectively. Searched ranges of μ and r/R in these figures are within $0\leq\mu\leq30°$ and $0\leq r/R\leq2$, respectively. Note that this range of μ covers the whole possible cases and that the range of r/R is retricted by considering difficulties in its implementation. From these figures, it can be observed that as R_{tz} gets smaller, the slope of the isotropic index with respect to the variations of those two parameters around the optimal region becomes steeper. On the contrary, as the value of R_{tz} increases, the optimal value of performance index decreases more or less but its gradient around the optimal configuration is shown to become much smoother.

Figure 5 shows the integrated contour plot for three design parameters. That is, constant contour lines of isotropic index of 1/2 (from each contour plots for the values of $R_{tz}=0.1$, 0.2, ···, 1) are integrated into one plot. From Figs. 2, 3 and 4, it can be expected that optimal value of R_{tz} lies close to 0.

Table 1 shows summary of optimization results when isotropic index (σ_{KI}) of normalized matrix

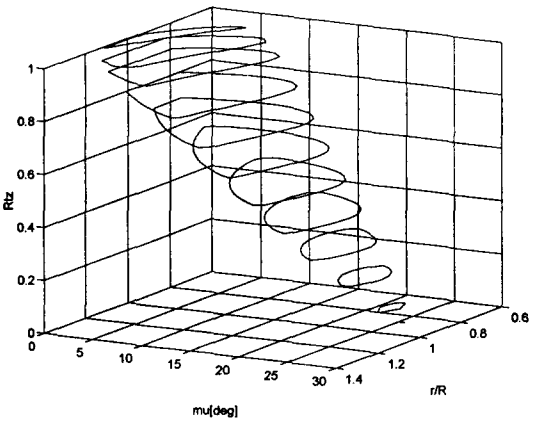

Fig. 5 Integrated contour plot of $\sigma_{KI}([G_u^t])=1/2$ with respect to R_{tz}.

$[S][G_u^t]^T[K]$ as in Eq. (58) is selected as a performance index. From this table, it can be confirmed that the optimal value for R_{tz} is less than $R_{tz}=0.01$ and that optimal value of performance index is 0.7. However, it should be noted that some of results are not practical, since R_{tz} is too small to realize as mentioned previously and around these optimal configurations, the gradient of performance index are very steep.

Up to now, optimal design are investigated, especially, for the case that the nominal force-to-torque ratio at the center of the upper plate is assumed to be 1 : 1. When nominal output force-

Table 1 Summary of optimization results with respect to r/R, μ, R_{tz} when $\alpha=0°$

R_{tz}	0.01	0.1	0.2	0.3	0.4	0.5	0.6	0.7	0.8	0.9	1.0	1.1	1.2	1.3	1.4	1.5
r/R	1.000	0.995	0.981	0.964	0.942	0.916	0.945	0.956	0.906	1.025	1.000	0.889	0.814	0.743	0.670	0.677
μ[deg]	29.71	27.13	24.24	21.03	18.13	15.42	10.55	7.31	6.16	1.30	0.00	0.30	0.11	0.00	0.14	0.00
PI(σ_{KI})	0.707	0.704	0.693	0.677	0.657	0.633	0.606	0.579	0.552	0.526	0.500	0.476	0.453	0.431	0.411	0.391

Table 2 Summary of optimization with respect to f_{max}/τ_{max}, r/R, μ, R_{tz} when $\alpha=0°$

$\frac{f_{max}}{\tau_{max}}$	$\frac{1}{10}$	$\frac{1}{7}$	$\frac{1}{5}$	$\frac{1}{3}$	$\frac{1}{2}$	1	2	3	5	7	10
R_{tz}	0.200	0.200	0.200	0.200	0.200	0.200	0.866	0.888	0.905	0.913	0.918
r/R	1.033	1.026	1.024	1.007	1.016	0.982	0.500	0.342	0.029	0.151	0.106
μ[deg]	21.15	23.40	23.54	25.77	23.54	24.13	0.00	0.00	0.00	0.00	0.00
PI(σ_{KI})	0.071	0.101	0.141	0.235	0.352	0.693	0.707	0.645	0.599	0.581	0.567

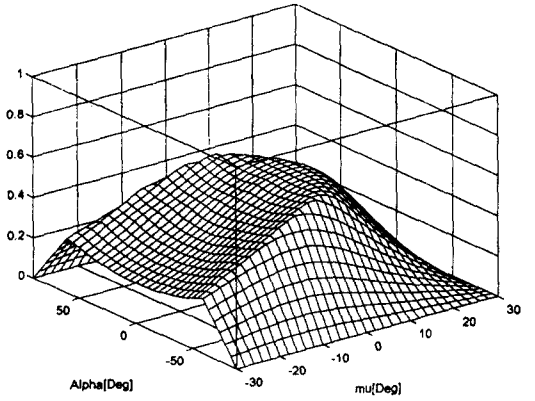

Fig. 6 Contour plot of $\sigma_{KI}([G_u^I])$ with respect to α and μ for $R_{tz}=0.8$ and $r/R=0.9$

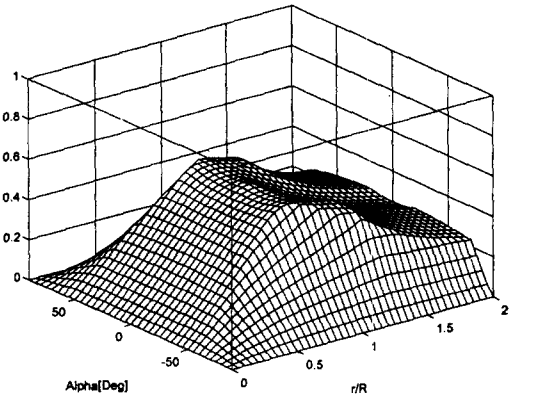

Fig. 7 Contour plot of $\sigma_{KI}([G_u^I])$ with respect to α and r/R for $R_{tz}=0.8$ and $\mu=0°$

to-torque ratio is varied, appropriate scale matrix should be applied to Eq. (58). Table 2 shows the summary of results from those optimizations, where another constraint on R_{tz}(i.e., $R_{tz}\geq 0.2$) is applied to optimization, noting that the radius-to-thickness ratio of the F/T sensors should not be too small for its implimentation.

When each of six prismatic bars has different length or shape, or is made of the different materials while maintaining the unit magnitude of stiffness along axial direction, the restriction on α ($\alpha=0°$) in optimization can not be applied any more. Figures. 6, 7 and 8 represent 3-D plots of isotropic indices of $[G_u^I]$ with respect to two different design variables when the other two variables are fixed. From these figures, it can be observed that there are a few local optimum points with respect to α, more specifically, around $\alpha=0°$, $-50°$, $50°$. When the value of α is varied within $-50°<\alpha<50°$, the value of optimal performance index is not varying significantly, compared with the other three design variables. But it can be noted that effect of α can not be neglected especially as R_{tz} gets smaller.

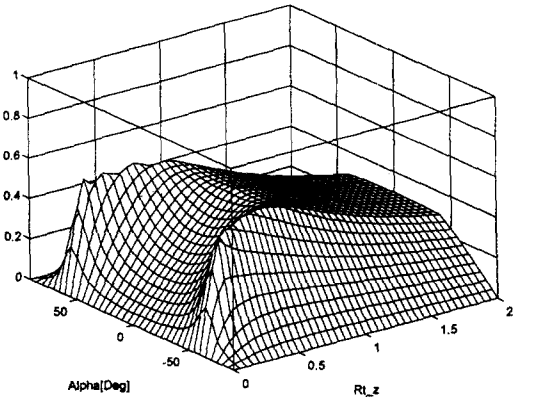

Fig. 8 Contour plot of $\sigma_{KI}([G_u^I])$ with respect to α and R_{tz} for $\mu=0°$ and $r/R=0.9$

Table 3 shows the summary of results of optimiza-

Table 3 Summary of optimization with respect to α, r/R, μ, R_{tz}

$\frac{f_{max}}{\tau_{max}}$	$\frac{1}{10}$	$\frac{1}{7}$	$\frac{1}{5}$	$\frac{1}{3}$	$\frac{1}{2}$	1	2	3	5	7	10
R_{tz}	0.200	0.200	0.200	0.200	0.200	0.200	0.485	0.605	0.905	0.913	0.918
r/R	1.033	1.024	1.024	1.007	1.016	0.981	0.689	0.468	0.029	0.151	0.106
μ[deg]	21.15	23.40	23.54	25.77	23.54	20.27	0.00	0.00	0.00	0.00	0.00
α[deg]	0.00	0.00	0.00	0.00	0.00	15.79	52.53	51.26	0.000	0.000	0.000
PI(σ_{KI})	0.071	0.101	0.141	0.235	0.352	0.693	0.795	0.668	0.599	0.581	0.567

tion with respect to four design parameters including α, when different values of desirable output force-to-torque ratios are used.

6. Conclusion

In this study, optimal design of a F/T sensor using Stewart Platform structure is discussed. This F/T sensor replaced the prismatic joints of Stewart platform by prismatic bars, which are deformable only along the axial direction. The complete kinematic analyses for the design of this kind of F/T sensor are conducted: that is, the position analysis, the first-order and the second-order kinematic analyses, and force-deformation analysis based on the first-order kinematic characteristics of the system. Lastly, dimensional syntheses for the F/T sensor are performed based on the isotropic index of the normalized matrix. First, optimizations are conducted with respect to three and four design parameters for the case that all six prismatic bars have the unit magnitude of stiffness only along axial direction. Optimizations are not conducted for the cases that each of prismatic bars has different stiffness or different length or that it is made of different materials in this study, but they can be performed by simply adjusting the performance index appropriately.

The implementation aspects are not discussed in this study. Currently, various aspects such as how to implement frictionless intersection joints connecting each plate with prismatic bars and what materials prismatic bars should be made of, and what shape they have, etc. are being investigated. The results and/or procedure obtained in this study can be easily employed with minor modifications at its final design stage.

References

Freeman, R. A. and Tesar, D., 1988, "Dynamic Modeling of Serial and Parallel Mechanisms/ Robotic Systems, Part I : Methodology, Part II : Applications," *Trends and Developments in Mechanisms, Machines, and Robotics, 20th Biennial Mechanism Conf., Kissimmee, FL, DE*. Vol. 15-2, pp. 7~21.

Kak, A. C. and Albus, J. S., 1985, "Sensors for Intelligent Robots," Chap. 13. in *Handbook of Industrial Robotics*, edited by Shimon Y. Nof, published by John Wiley & Sons.

Kim, W. K., Huh, K. K., Huh, H., 1993, "Analysis of Wrist-Type 6-Degree-of-Freedom Force/ Torque Sensors Based on Stewart Platform Structure," *Journal of Korea-University Science and Technology Institute*, Vol. 1., pp. 57~74.

Kim, W. K,, 1994, Huh, K. K., Yi, B. J. and Cho, W., "Optimal Design of Wrist-Type 6-Degree-of-Freedom Force/Torque Sensors Based on Stewart Platform Structure," *Proceedings of KSME Spring Conference*, pp. 668~673.

Kozo Ono and Yotaro Hatamura, 1986, "A New design For 6-Component Force/Torque Sensors," *Proceedings of the XIth International Conference on Measurement of Froce and Mass, Amsterdam*, The Netherlands, pp. 39~48.

Ma, O. and Angeles, J., 1992, "Architecture Singularities of of Parallel Manipulators," *Int'l Journal of Robotics and Automation*, Vol. 7., No. 1, pp. 23~29.

Nakamura, Y., Yoshikawa, T. and Futamata, I., "Design and Signal Processing of Six-Axis Force Sensors."

Nguyen, C. C., Antrazi, S. S., Zhou, Z. L. and Campbell, Jr, C.E., 1992, "Analysis and Experimentation of Stewart Platform-Based Force/Torque Sensor," *Int'l Journal of Robotics and Automation*, Vol. 7, No. 3, pp. 133~140.

Reboulet, C. and Pigeyre, R., 1992., "Hybrid Control of a 6-DOF In-Parallel Actuated Micro-Manipulator Mounted on a SCARA Robot," *IEEE Int'l Journal of Robotics and Automation*, Vol. 7, No. 1, pp. 10~14.

Shimano, B. and Roth, B., 1978, "On Force Sensing Information and Its Use in Controlling Manipulator," *Proc. of the 8th Industrial Symposium on Industrial Robots*, Washington, D.C. pp. 119~126.

Svinin, M. M. and Uchiyama, M., 1994, "Analytical Models for Designing Force Sensors," *Proceeding of IEEE Conference, Robotics and Automation*, pp. 1778~1783.

Uchiyama, M., Nakamura, Y. and Hakomori, K., 1991, "Evaluation of the Robot Force Sensor

Structure Using Singular Value Decomposition," Advanced Robotics, Vol. 5, No. 1, pp. 39~52.

Yabuki, A., 1990, "Six-Axis Force/Torque Sensor for Assembly Robots," *Fujitsu Sci. Tech. J.*, Vol. 26, No. 1., pp. 41~47.

Yoshida, T., 1984, "6-Component Force Transducer and Its Application," *Proceedings of the 10th conference of IMERO TC3 on Measurement of Force and Mass*, Japan, Sep., pp. 11~15.

Yoshikawa, T. and Miyazaki, T., 1989, "A Six-Axis Force Sensor with Three-Dimensional Cross-Shape Structure," *IEEE int'l conf. on Robotics and Automation*, pp. 249~255.